

SQUID-on-tip with single-electron spin sensitivity for high-field and ultra-low temperature nanomagnetic imaging

Y. Anahory^{1*}, H.R. Naren², E.O. Lachman², S. Buhbut Sinai³, A. Uri²,
L. Embon², E. Yaakobi², Y. Myasoedov², M.E. Huber⁴, R. Klajn³ and E. Zeldov²

¹Racah Institute of Physics, The Hebrew University, Jerusalem 91904, Israel

²Department of Condensed Matter Physics, Weizmann Institute of Science, Rehovot
7610001, Israel

³Department of Organic Chemistry, Weizmann Institute of Science, Rehovot 7610001, Israel

⁴Departments of Physics and Electrical Engineering, University of Colorado Denver, Denver
80217, USA

*Corresponding author: yonathan.anahory@mail.huji.ac.il

Scanning nanoscale superconducting quantum interference devices (nanoSQUIDs) are of growing interest for highly sensitive quantitative imaging of magnetic, spintronic, and transport properties of low-dimensional systems. Utilizing specifically designed grooved quartz capillaries pulled into a sharp pipette, we have fabricated the smallest SQUID-on-tip (SOT) devices with effective diameters down to 39 nm. Integration of a resistive shunt in close proximity to the pipette apex combined with self-aligned deposition of In and Sn, have resulted in SOT with a flux noise of $42 \text{ n}\Phi_0\text{Hz}^{-1/2}$, yielding a record low spin noise of $0.29 \mu_B\text{Hz}^{-1/2}$. In addition, the new SOTs function at sub-Kelvin temperatures and in high magnetic fields of over 2.5 T. Integrating the SOTs into a scanning probe microscope allowed us to image the stray field of a single Fe_3O_4 nanocube at 300 mK. Our results show that the easy magnetization axis direction undergoes a transition from the (111) direction at room temperature to an in-plane orientation, which could be attributed to the Verwey phase transition in Fe_3O_4 .

Nanoscale magnetic imaging is gaining interest in recent years in diverse fields of research and applications, including biological, chemical, and physical systems¹⁻³. The quest for quantitative mapping of extremely weak local magnetic signals has driven development of very sensitive new techniques, including cold atom chips⁴, scanning nitrogen-vacancy diamond magnetometers^{2,5-8}, and scanning micro- and nano-superconducting quantum interference devices (SQUIDs)⁹⁻¹⁵. These tools have been employed for quantitative imaging of microscopic static and dynamic magnetic structures^{6,16-20}, current imaging^{7,21,22}, and responses to local perturbations^{23,24}. Many of the systems of current interest in condensed matter physics, however, including topological states of matter, fractional quantum Hall, spin ice, and unconventional superconductivity, often require imaging at high spatial resolution with high spin sensitivity at sub-Kelvin temperatures and at high magnetic fields. These conditions are currently inaccessible by most of the existing imaging techniques. In this work, we present the development of scanning nanoSQUIDs that operate at sub-Kelvin temperatures and significantly expand the state-of-the-art at these temperatures in terms of spatial resolution, spin sensitivity, and applied magnetic fields.

Previously, we have developed a highly sensitive scanning probe microscope based on a nanoscale SQUID that resides at the apex of a sharp tip (SQUID-on-tip, or SOT)^{14,25,26} and utilized the technique for the study of vortex dynamics^{19,27}, nanoscale magnetism in topological insulators^{28,29}, and superparamagnetism at oxide interfaces¹⁸. The SOT devices made of Pb attain loop diameters down to 46 nm and display extremely low flux noise of $50 \text{ n}\Phi_0\text{Hz}^{-1/2}$ and record spin sensitivity of $0.38 \mu\text{BHz}^{-1/2}$ at 4.2 K¹⁴. In addition, the Pb SOTs show an extremely high thermal sensitivity of below $1 \mu\text{K}\cdot\text{Hz}^{-1/2}$, allowing nanoscale imaging of dissipation mechanisms in quantum systems. Such imaging reveals the minute quantity of heat generated by inelastic scattering of electrons from a single atomic defect^{30,31}. At sub-Kelvin temperatures, however, the Pb SOTs become highly hysteretic due to an increase in the critical current I_c and thermal instabilities. As a result, these SOTs with outstanding sensitivity at 4.2 K are barely useable at ultra-low temperatures. SOTs made of Al were shown to operate at sub-Kelvin temperatures²⁵, but they display a significantly higher noise of $2 \mu\Phi_0\text{Hz}^{-1/2}$ due to high kinetic inductance and their operation is limited to magnetic fields of below $\sim 0.5 \text{ T}$.

To improve the sensitivity, spatial resolution, and operating range of temperatures and magnetic fields of the SOT, we describe here a number of technological advancements, including *i*) incorporation of grooved quartz pipettes, *ii*) reduction of SOT diameter, *iii*) integration of a resistive shunt on the tip and *iv*) development of SOTs made of In and Sn.

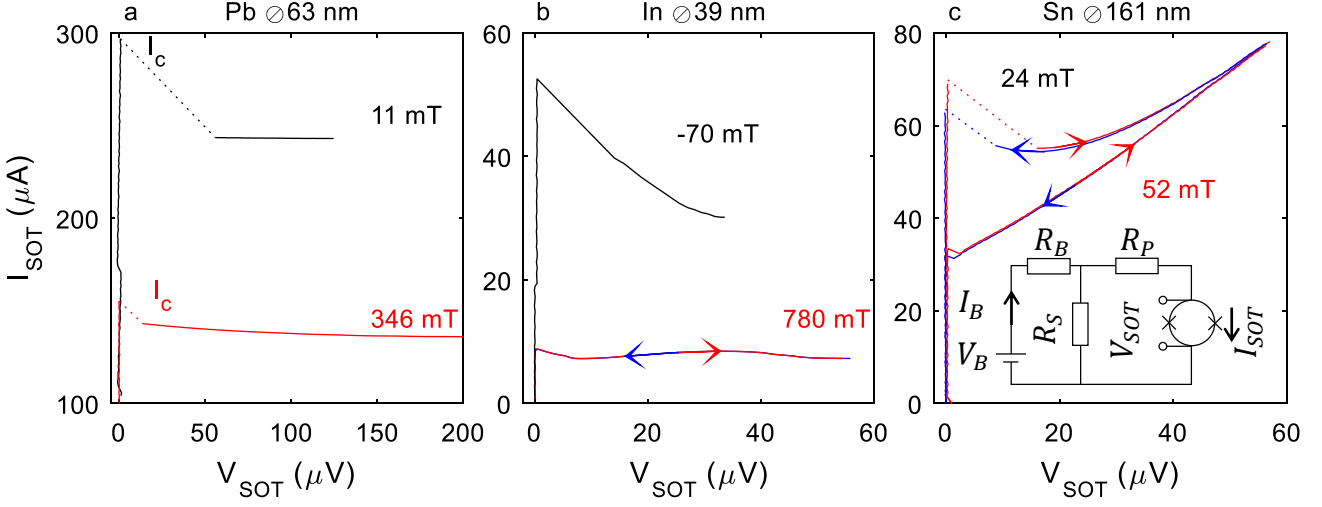


Figure 1. I - V characteristics of SOT devices made of different materials at 300 mK. (a-f) I - V characteristics of three different SOT devices at two different applied magnetic fields. (a) I_{SOT} - V_{SOT} curve of a hysteretic unshunted Pb SOT with diameter of 63 nm ($R_B = 2.0$ k Ω , $R_S = 3.0$ Ω , $R_P = 3.1$ Ω). (b) I_{SOT} - V_{SOT} characteristics of an In SOT of 39 nm diameter with integrated shunt-on-tip ($R_B = 7.0$ k Ω , $R_S = 3.0$ Ω , $R_P = 1.8$ Ω). The red (blue) curve shows the measurement upon ramping I_B up (down). (c) I_{SOT} - V_{SOT} characteristics of a slightly hysteretic shunted Sn SOT with diameter of 161 nm ($R_B = 7.0$ k Ω , $R_S = 3.0$ Ω , $R_P = 1.8$ Ω). The inset shows a simplified diagram of the measurement circuit.

To illustrate the limitations of Pb SOTs at ultra-low temperature, we inspect their current-voltage (I - V) characteristics. Figure 1a shows typical I_{SOT} - V_{SOT} curves of a Pb SOT at two different applied fields at 300 mK. The measurement circuit, illustrated schematically in the inset of Fig. 1c, consists of a room temperature voltage source that provides the bias current I_B through the low temperature bias resistor R_B with typical resistance of a few k Ω . The SOT is effectively voltage biased by the low resistance shunt resistor R_S of a few Ω in presence of a parasitic resistance R_P . More data and details about the measurements are shown in the electronic supplementary information (ESI). The I_{SOT} - V_{SOT} curves can be separated into two parts. Below I_c , the SOT is superconducting and V_{SOT} is zero, while for larger values of I_{SOT} , the SOT is in the voltage state. The I_{SOT} - V_{SOT} curve of the SOT in Fig. 1b shows that, once the critical current I_c is reached, the voltage jumps discontinuously to a large value of 55 μ V (dashed line) with I_{SOT} showing almost no dependence on the bias above I_c . In this hysteretic state, the differential resistance (dV_{SOT}/dI_{SOT}) is too high to be measured accurately with our circuit. Its value, on the order of several tens of ohms, indicates that the SQUID loop and part of the leads are in the normal state. In this state, the SOT cannot serve as a sensitive magnetometer. To circumvent this problem, the SOT characteristics must be damped to attain non-hysteretic behavior.

An important parameter to consider for identifying the cause of the hysteresis is the Stewart-McCumber parameter $\beta_c = 2\pi I_c R^2 C / \Phi_0$, where R and C are the normal resistance and capacitance of the Josephson junction, respectively, and Φ_0 is the flux quantum. This parameter is derived from the resistively and capacitively shunted junction (RCSJ) model³² and provides a qualitative description of the SOT. For $\beta_c > 1$, the Josephson junctions are underdamped and likely to be hysteretic. However,

when $\beta_c < 1$, the desired overdamped non-hysteretic characteristics are expected. For $I_c = 300 \mu\text{A}$ and an estimated $C \cong 2 \text{ fF}$ and $R \cong 50 \Omega$, we obtain $\beta_c \cong 5$ for the Pb SOT in Figs. 1a,b. This result indicates that the β_c parameter should be reduced by a factor of ~ 10 by decreasing R and/or I_c to prevent hysteresis.

We first consider the possibilities of reducing I_c . I_c can be reduced *in-situ* by increasing the temperature. Indeed, we find that the Pb SOTs hysteretic at 300 mK usually become non-hysteretic above 4 K. Here, however, our goal is to attain sensitive operation at ultra-low temperatures. The second possibility for *in-situ* reduction of I_c is the application of high magnetic fields. As we show below, the Pb SOT indeed becomes non-hysteretic at fields above $\sim 1.5 \text{ T}$. This approach, however, is not applicable if low- or variable-field operation is required.

The most straightforward means for reducing I_c is reducing the thickness of the superconducting film forming the SQUID loop. This approach, however, does not work reliably for Pb films, which show significant surface roughness, and therefore requires a minimum film thickness to attain superconducting percolation. We therefore aim to employ other superconducting materials with a lower critical temperature T_c in order to attain lower I_c at sub-Kelvin temperatures. We have accordingly developed a technique to deposit In and Sn thin films onto the quartz pipette. In order to overcome the high room-temperature surface mobility of In and Sn, which results in island growth rather than a continuous thin film, we utilized a high-vacuum system with an *in-situ* rotatable ^4He cryostat for thermal deposition of In and Sn onto cryogenically cooled tips. This technique is similar to that used to make Pb SOTs and is discussed in Ref. 14. Scanning electron micrographs of the resulting In and Sn SOTs are shown in Figs. 2e-g.

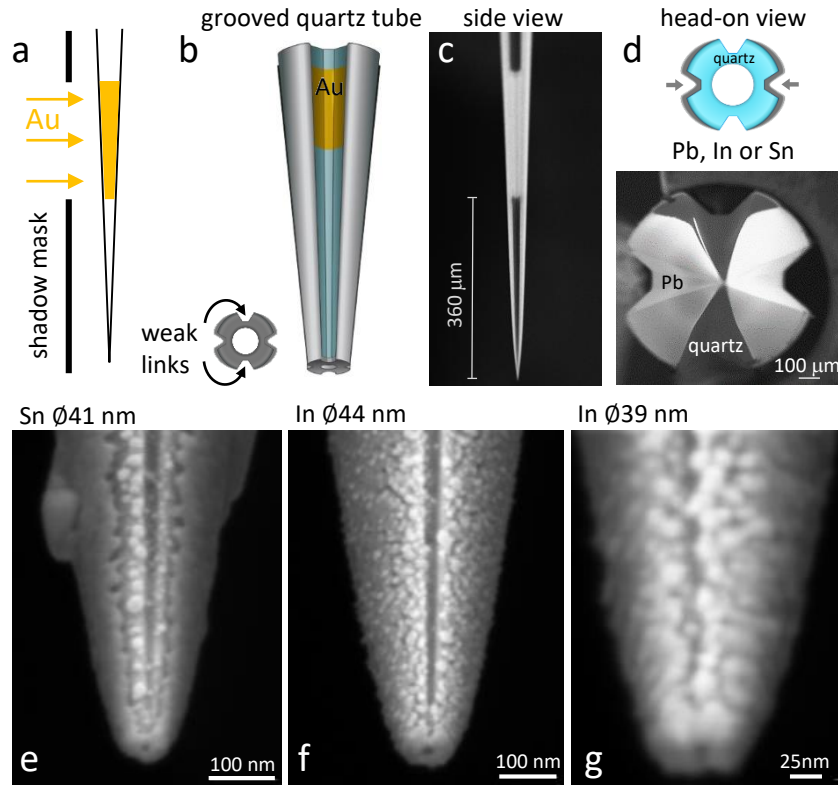


Figure 2. Fabrication of shunted Sn and In SOT devices on grooved pipettes. (a) Schematic drawing of the fabrication process of the shunt-on-tip using Au deposition through an aperture in a shadow mask. (b) Schematic drawing of the final SOT structure. The pipette is fabricated by laser pulling of a quartz capillary with four grooves along its length. Following deposition of the shunt-on-tip, two superconducting leads are deposited on two opposite sides of the pipette (grey) and a third head-on deposition is used to coat the apex of the pipette, forming the SQUID loop. The inset shows the apex viewed from below coated with a superconductor (grey) with two weak links formed at the constrictions. (c) SEM side view image of the final SOT structure showing the metallic layers in bright (Au shunt-on-tip and the In side electrodes) and the bare quartz in dark. The length of the shunt-on-tip is 250 μm and it is located 360 μm away from the tip apex (shown in (e-g)). (d) Schematic cross section of the quartz capillary (blue) with superconducting leads (grey) on the two sides (top). Low-magnification SEM head-on image (bottom) showing the grooved pipette (1 mm outer diameter) with Pb leads on two opposite sides (bright) extending all the way to the apex in the center. (e-g) SEM images of different SOT devices made of Sn (e) and In (f,g) with effective diameters of 41 (e), 44 (f), and 39 nm (g). The quantum interference patterns of devices (f) and (g) are shown in Figs. 3b and 3c respectively.

An additional approach for reducing β_c is the reduction of R . In fact, this method is expected to have a larger influence on β_c since $\beta_c \propto R^2$. Since the normal state resistance of the superconducting film cannot be varied independently of I_c , we incorporate a shunt resistor integrated with the SOT. At the relevant Josephson frequencies ($\gtrsim 1$ GHz), an inherent impedance mismatch exists between the SOT and the long (~ 1 cm) and narrow leads along the pipette; any external shunt resistor would have little effect due to this high-series impedance. To avoid this situation, the shunt resistor must be incorporated on the pipette in close vicinity to the SQUID loop. Depositing a normal metal directly onto the apex of the tip could reduce R . However, because of the small loop size, it is not possible, on the

apex itself, to achieve a thickness that would reduce the normal resistance significantly. Moreover, in this configuration, we found that the inverse proximity effect³³ significantly suppresses the superconductivity in the SQUID loop. Taking into account these design limitations, we have developed a shunt-on-tip as shown in Fig. 2. Using a shadow mask (Fig. 2a), a thin film of Cr/Au (~ 5 nm/ ~ 10 nm) is deposited on the bare quartz pipette forming a strip ~ 250 μm long at a distance of ~ 400 μm from the apex (Fig. 2b,c). After the subsequent self-aligned deposition of the superconducting leads (Fig. 2d), this metallic film acts as a resistive shunt between the two leads. By tuning the thickness and the length of the Cr/Au film the desired resistance in the range of 2 to 10 Ω can be attained. We find that although the sole addition of the shunt-on-tip could not solve the hysteresis problem for a Pb SOT ($I_c \sim 250$ μA), it is a crucial design and fabrication parameter to control undesirable hysteresis specifically with Sn and In SOTs and with Pb SOTs at elevated fields when $I_c \lesssim 100$ μA . The shunt-on-tip also has the added benefit of protecting the SOT from static discharge while the device is at room temperature.

Sn and In SOTs fabricated with the integrated shunt-on-tip as described above were characterized at 300 mK. Typical I_{SOT} - V_{SOT} curves are shown in Figs. 1a-c. Their critical currents are about five times lower than in Pb devices (Fig. 1a). In addition, the Au shunt-on-tip lowers significantly the normal state resistance. For example, the Sn SOT in Fig. 1c shows a differential resistance of 0.9 Ω at high bias. The combination of a lower I_c and reduced R eliminates the hysteresis as shown by the ramp up (red) and ramp down (blue) characteristics in Figs. 1c.

An additional goal of this work was to reduce the SOT diameter, which has two advantages. The first is improved spatial resolution for scanning magnetic imaging. The second is reduced spin noise, aiming at attaining single-electron spin sensitivity or better. A SQUID is fundamentally characterized by its flux noise $S_\Phi^{1/2}$. The corresponding field noise in the case of a uniform magnetic field is given by $S_B^{1/2} = S_\Phi^{1/2}/(\pi r^2)$, which decreases as $1/r^2$, where r is the SQUID radius. Large SQUIDs are therefore preferable for sensitive measurements of uniform magnetic fields. Scanning nanoscale microscopy, however, requires imaging of spatially varying magnetic fields and resolving their local sources, in particular magnetic dipoles. In this case, the relevant performance metric is magnetic dipole, or spin, sensitivity. Assuming that the spin is located in the center of the SQUID, the spin sensitivity in units of $\mu_B \cdot \text{Hz}^{-1/2}$ is given by $S_n^{1/2} = S_\Phi^{1/2} r/r_e$, where $S_\Phi^{1/2}$ is in units of $\Phi_0/\text{Hz}^{1/2}$ and $r_e = 2.82 \times 10^{-15}$ m is the classical electron radius³⁴. Since $S_n^{1/2} \propto r$, smaller SQUIDs achieve a lower spin noise.

The limiting factor in the fabrication of ultra-small SOTs is maintaining a gap between the superconducting leads along the pipette. SOT fabrication is based on a self-aligned process in which the superconducting leads are formed by two side-depositions, followed by a third head-on deposition step coating the tip apex^{14,25}. In conventional uniformly circular capillaries, as the diameter of the pipette is reduced, the gap size is reduced proportionally, leading eventually to formation of shorts and additional Josephson junctions between the leads. In order to maintain a sufficient gap between the leads, we have employed a quartz capillary with four grooves³⁵ along its length as depicted in Fig. 2b,d. These grooves maintain their original shape during the pipette pulling process and provide shadowing during the first two deposition steps, resulting in a well-defined gap down to smaller pipette diameters than is possible for a uniform capillary. For this purpose, two grooves on the opposite sides of the pipette would have been sufficient. However, pulling a capillary with two grooves results in a pipette with an oval cross section. Therefore, in order to maintain a circular shape, four symmetric

grooves were used as shown in Fig. 2. Employing this approach, we have attained a nanoSQUID with a record small effective diameter of 39 nm depicted in Fig. 2g.

The grooves have the additional advantage of reducing the effective width and length of the two weak link nano-constrictions (Fig. 2b inset). Tuning the nano-constrictions dimensions could be used to tune I_c and β_c , as well as the kinetic inductance of the junctions for better modulation depth and improved flux noise. Thus, the depth of the grooves and their shape can be designed to attain optimal performance of the SOT.

The quantum interference patterns of the various SOT devices, measured at 300 mK, are presented in Fig. 3. The Sn SOT with an effective diameter of 161 nm shows a number of oscillation periods with an envelope of decreasing I_c that vanishes at the upper critical field H_{c2} of about 0.4 T (Fig. 3a). The period of the quantum oscillations increases with decreasing SOT diameter. As a result, in the smaller In devices, only the central lobe of the interference pattern is fully visible (Figs. 3b,c), while the following lobes are truncated by H_{c2} . The In SOT presented in Fig. 2g shows a quantum oscillation period of $\mu_0\Delta H_z = 1.69$ T (Fig. 3c). From this period we calculate the effective diameter $d = (4\Phi_0/\pi\mu_0\Delta H_z)^{1/2} = 39$ nm. This constitutes the smallest SOT reported to date¹⁴.

The operation of many SQUIDs is limited to relatively low fields due to penetration of vortices into the SQUID loop. In SOTs, in contrast, the width of the SQUID loop is usually smaller than the coherence length and the leads are aligned essentially parallel to the applied field, preventing vortex penetration. As a result, the SOTs can operate in applied fields of up to H_{c2} . The 44 nm diameter In SOT in Fig. 3b shows an interference pattern up to a record high field of 1.9 T. Even higher field operation can be attained with Pb SOTs. At 300 mK, the Pb SOTs are not useable below about 1.5 T due to too high critical current causing hysteretic behavior. However, as a result of the suppression of I_c with magnetic field, operation in fields of up to almost 3 T can be attained as demonstrated in Fig. 3d for $d = 65$ nm Pb SOT. Here we show for clarity the tip response to magnetic field, $dI_{SOT}/d(\mu_0H_z)$, which is directly related to the device sensitivity.

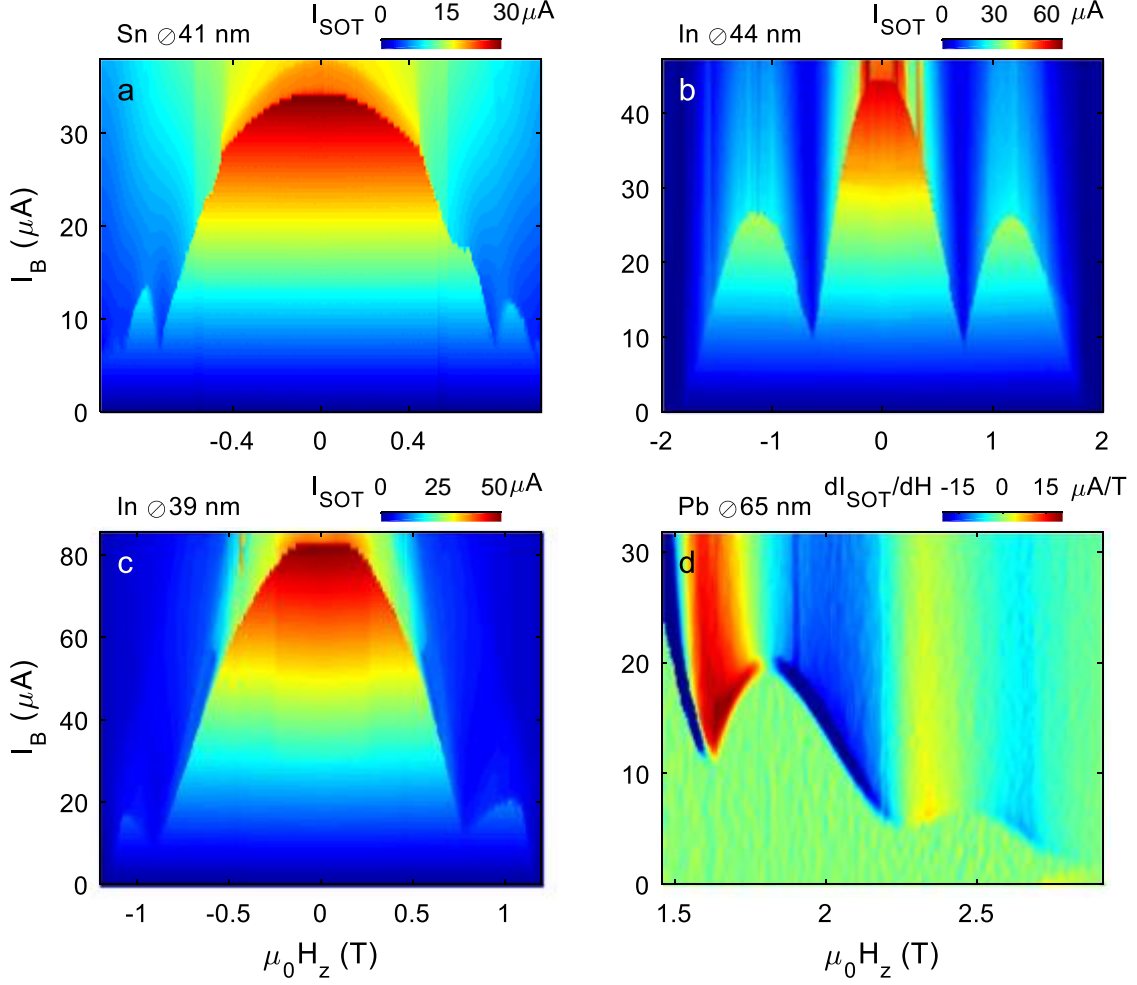


Figure 3. Quantum interference patterns of four SOT devices at 300 mK. (a-c) Color rendering of I_{SOT} - V_B characteristics vs. applied field $\mu_0 H_z$. (a) Sn SOT with an effective diameter $d = 41$ nm ($\mu_0 \Delta H_z = 1.53$ T) measured using the circuit in Fig. 1f with $R_B = 7.0$ k Ω , and $R_S = 3.0$ Ω . (b) Same as (a) for an In SOT with $d = 44$ nm ($\mu_0 \Delta H_z = 1.37$ T), $R_B = 6$ k Ω , and $R_S = 1$ Ω . (c) Same as (a) for an In SOT of $d = 39$ nm ($\mu_0 \Delta H_z = 1.69$ T), $R_B = 7.0$ k Ω , and $R_S = 3.0$ Ω . (d) Derivative of I_{SOT} with respect to $\mu_0 H_z$ presenting the response function of a Pb SOT with $d = 65$ nm ($\mu_0 \Delta H_z = 0.63$ T) at elevated fields, $R_B = 11$ k Ω , and $R_S = 1.4$ Ω .

The flux sensitivity of the SOT is determined by dividing the current spectral noise density in units of $AHz^{-1/2}$ by the transfer function $dI_{SOT}/d\Phi$, where Φ is the magnetic flux penetrating through the SQUID loop. The resulting flux noise is shown in Fig. 4 for the 39 nm device at two different fields, 0.74 T (red) and 1.1 T (blue). Above 3 kHz, the noise becomes essentially frequency-independent and we attain flux noise as low as $S_{\Phi}^{1/2} = 42$ n $\Phi_0 Hz^{-1/2}$ at 0.74 T and 45 n $\Phi_0 Hz^{-1/2}$ at 1.1 T. Remarkably, this device reaches a spin sensitivity of 0.29 and 0.31 $\mu_B Hz^{-1/2}$ at 0.74 and 1.1 T respectively, which makes it the most sensitive SQUID in terms of spin noise reported to date¹⁴.

The In device with $d = 44$ nm shown in Figs. 2c and 3b also achieved impressive flux and spin sensitivity values of 145 n $\Phi_0/Hz^{1/2}$ and 1.1 $\mu_B Hz^{-1/2}$ respectively at a field of 1.87 T. The Sn SOTs did not show any significant advantage over In SOTs in terms of sensitivity or operating magnetic fields. Nonetheless, the use of Sn may prove to have practical advantage since it oxidizes less than In and hence Sn SOTs may have a longer shelf life.

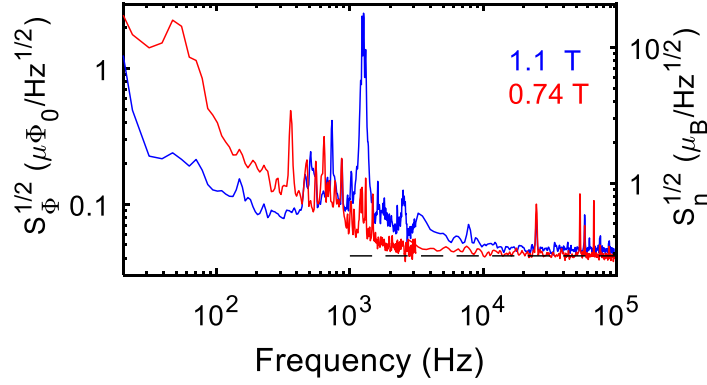


Figure 4. Flux and spin noise spectral densities of Ø39 nm In SOT at 300 mK. The $S_{\Phi}^{1/2}$ (left axis) and $S_n^{1/2}$ (right axis) are shown for applied field of 0.74 T (red) and 1.1 T (blue). The excess noise around 1 kHz is due to experimental setup. In the white noise region above 3 kHz the flux noise reaches $42 \text{ n}\Phi_0\text{Hz}^{-1/2}$ and the spin noise $0.29 \text{ }\mu_B\text{Hz}^{-1/2}$, which is the lowest ever reported for a SQUID.

To demonstrate the utility of the improved devices, an In SOT was used to investigate the low-temperature magnetic properties of single magnetite (Fe_3O_4) nanocubes. Bulk measurements at room temperature have shown that the easy magnetization axis of magnetite is in the $\langle 111 \rangle$ direction^{36,37}, which corresponds to the body diagonals of the cube^{38,39}. Below $T_V \sim 120 \text{ K}$, there is an abrupt change in many of the physical properties of the material such as the electrical conductivity, specific heat, lattice structure, and magnetization⁴⁰. This so-called Verwey transition is believed to be caused by a long-range charge order^{41,42} and has motivated many studies of size effects in nanocrystals^{43–46} and thin films^{47,48} below T_V . Apart from an interest in the Verwey transition, there is a fundamental and technological interest in probing the effects of shape and size on magnetism^{17,49}. However, most magnetic characterization studies have been limited to large particle ensembles^{50,51} or to non-spatially resolved magnetic signals^{52–57}.

In order to probe the properties of individual nanocubes, a 150 nm diameter In SOT was integrated into a home-built scanning probe microscope operating at 300 mK⁵⁸ with the aim of resolving the spatial distribution of the out-of-plane component of the stray magnetic field $B_z(x, y)$. SQUIDs usually have regions of reduced or zero sensitivity (“blind spots”) at the interference pattern extrema. As a result, a SQUID with two perfectly symmetric arms is not sensitive at zero field. In this experiment, a larger device was used in order to yield a smaller interference pattern period, which translates into denser sensitive regions in the field domain. Combining that with an inherent device asymmetry leads to good sensitivity at zero applied field. Smaller SOTs (down to 43 nm) were used in other microscopy experiments recently published^{59,60} using the same improvements discussed in this work. Nanocubes of nominal average size $l \cong 13 \text{ nm}$ were synthesized as described in Ref. 39 and dropcasted onto a Si substrate. Figures 5a-d show the $B_z(x, y)$ images acquired at four different applied fields $\mu_0 H_z$. Prior to the first measurement, the magnetic field was raised to $\mu_0 H_z = 0.36 \text{ T}$ to calibrate the SOT and then decreased to zero. At $\mu_0 H_z = 0$ (Fig. 5a), the magnetization of the cube is almost perfectly aligned with the substrate plane. If the nanocube was magnetized along its diagonal axis, as at room temperature, this would imply that the cube is standing on one of its vertices, which is highly unlikely considering the strong van der Waals forces between the cube face and the substrate⁶¹ – indeed, high-resolution SEM imaging (Fig. 5l) confirmed that nanocubes are found with one face laying on the substrate³⁹. We therefore conclude that at $\mu_0 H_z = 0$ the magnetization of the nanocube at 300 mK occurs in the $\{100\}$ plane (cube face) and not in the $\langle 111 \rangle$ direction. Indeed, for bulk magnetite, it is known that for $T < T_V$, the easy magnetization axis changes from $\langle 111 \rangle$ to $\langle 100 \rangle$ ^{37,40}. It was also shown

that nanocubes synthesized by the same method are magnetized in the $\langle 111 \rangle$ direction at room temperature³⁸. Our nanoscale magnetic imaging thus provides a direct observation of the axis of preferential magnetization of a single, isolated nanocube below the Verwey transition.

Some nanocubes could have defects that may influence their magnetic state. We imaged four other nanocubes in this study (see ESI, Section 2) and found an in-plane magnetization of comparable magnitude. We did not observe any other magnetization orientation at zero-field, which is somewhat surprising since a purely out-of-plane magnetization would also be consistent with magnetization in the $\langle 100 \rangle$ direction. We speculate that an interaction with the underlying substrate is responsible for breaking this symmetry.

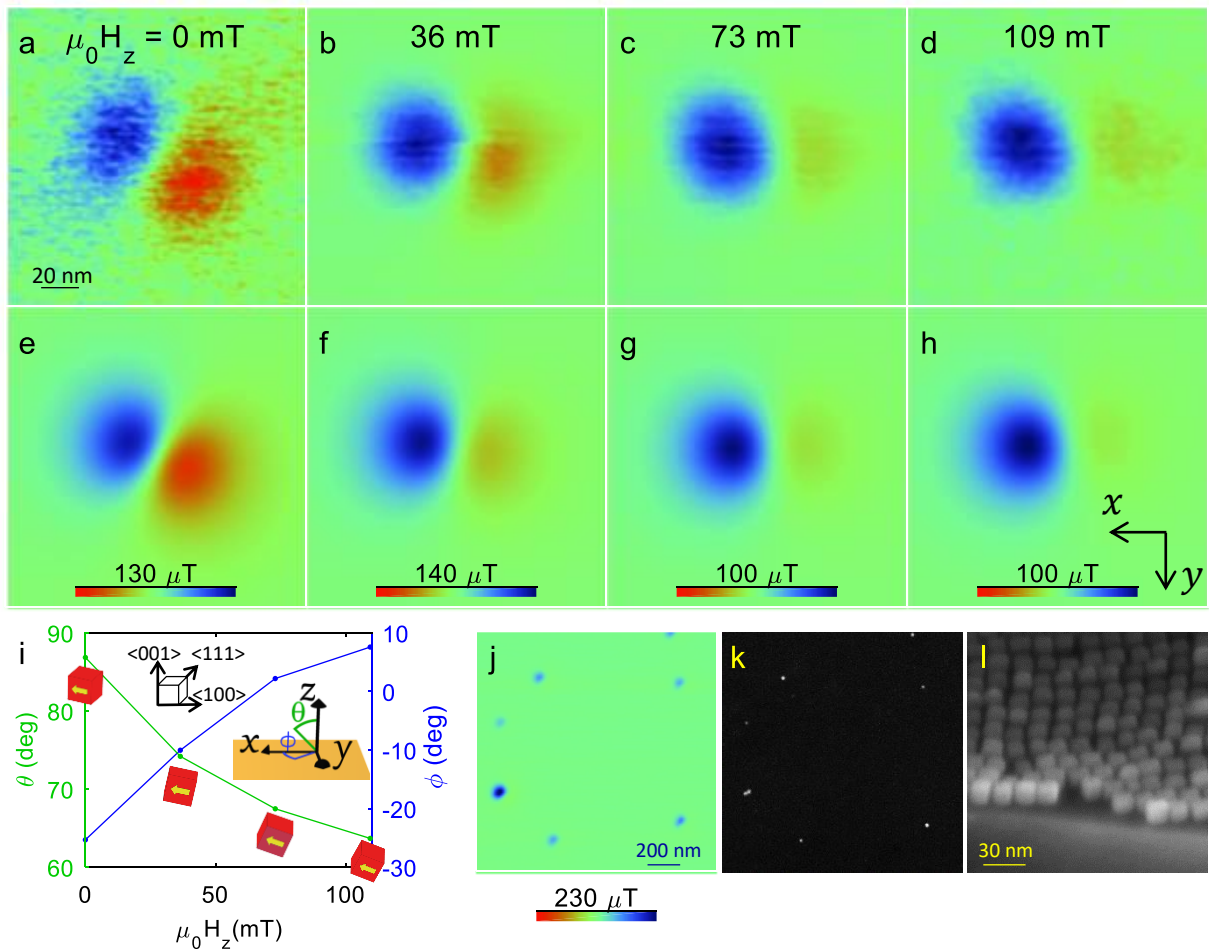


Figure 5. Low-temperature characterization of the magnetization of a single Fe_3O_4 nanocube. (a-d) Stray field $B_z(x, y)$ of a single Fe_3O_4 13 nm nanocube at $\mu_0 H_z = 0$ T (a), 36 mT (b), 73 mT (c), and 109 mT (d) at 300 mK. (e-h) Corresponding best fit numerically simulated $B_z(x, y)$ with a constant magnetic moment $m_0 = 2.3 \times 10^5 \mu_B$ and varying azimuthal and polar angles. (i) Polar angle θ (green) and azimuthal angle ϕ (blue) and as a function of the applied field as derived from the fitting procedure. The cubes in red indicate the out-of-plane tilting and rotation of the nanocube upon increasing the applied field while keeping the magnetization orientation fixed to the cube axes (yellow arrow). Right inset: coordinate system with respect to the substrate (orange). Top inset: the crystallographic directions of a nanocube. (j) Measured $B_z(x, y)$ of a few nanocubes on a Si substrate at 4.2 K and $\mu_0 H_z = 0.4$ T. The darker blue spot on the left corresponds to two nanocubes next to each other. (k) SEM image of the same field of view as in (j) showing the nanocubes in bright. (l) High-resolution SEM image of an array of nanocubes viewed at an angle.

Figures 5b-d show the measured $B_z(x, y)$ at $\mu_0 H_z = 36, 73,$ and 109 mT, respectively. For each of the images, the magnitude of the magnetic moment m_0 as well as its polar, θ , and azimuthal, ϕ , angles were derived by performing a numerical fit of the data. Our model comprises a finite size SQUID loop with fitting parameters m_0, θ, ϕ , and the SOT-to-nanocube distance. The corresponding numerically attained best-fit stray field maps are presented in Figs. 5e-h. We derive a magnetic moment of $m_0 = 2.3 \times 10^5 \mu_B$, which is quite consistent with the volume magnetization reported for Fe_3O_4 nanoparticles at low temperature⁵⁰. A larger-scale $B_z(x, y)$ image of seven nanocubes is shown in Fig. 5j. According to the SEM image of the same area (Fig. 5k), five nanocubes are well separated and two nanocubes on the left are bunched together, giving rise to the higher $B_z(x, y)$ signal (darker blue in Fig. 5j).

The derived angles θ and ϕ are shown in Fig. 5i. The out-of-plane component of the magnetization increases with increasing H_z , which can be attributed to either rotation of the magnetization orientation within the nanocube, or the rotation of the entire nanocube. The work W performed on the nanocube by the magnetic field from $\mu_0 H_z = 0$ to 0.109 T is $W = \mu_0 \int_{\theta_1}^{\theta_2} \vec{m} \times \vec{H} d\phi = 3 \times 10^{-20}$ J or 6 kJ/m³, which is smaller than the magnetocrystalline anisotropy required for the rotation of magnetization orientation⁶². This fact, combined with the continuous variation of the angles upon ramping the field up and down, suggests that, despite the van der Waals force that acts as a restoring force, the entire nanocube is tilted out of plane upon increasing the field rather than that the magnetization orientation is varied within a stationary nanocube. The azimuthal angle ϕ is also observed to change slightly with H_z . Interestingly, upon reducing H_z back to zero, the magnetic moment returned to the in-plane orientation, $\theta \sim 90^\circ$, but with a slightly different azimuthal angle, indicating that the nanocube “landed” with a slightly different in-plane orientation after the out-of-plane field-induced tilting. If the nanocube stayed still, we would expect the azimuthal angle of the magnetization to change by a multiples of 90° .

In conclusion, we have developed SQUID-on-tip devices made of In and Sn and have introduced grooved pipette geometry and an integrated resistive shunt on tip. These advances led to the smallest size In SOTs of 39 nm effective diameter, ultra-low flux noise of $42 \text{ n}\Phi_0\text{Hz}^{-1/2}$, record spin sensitivity of $0.29 \mu_B\text{Hz}^{-1/2}$, operation at ultra-low temperatures, as well as enhanced operating field of Pb SOTs up to over 2.5 T. The new devices were utilized to image the stray magnetic field generated by a single superparamagnetic Fe_3O_4 nanocube, revealing that the easy magnetization axis resides in the $\{100\}$ plane rather than in the $\langle 111 \rangle$ direction and providing a direct manifestation of the Verwey phase transition observed on a single nanocube level. The new generation of the SQUID-on-tip devices paves the way to nanoscale magnetic and thermal imaging of a wide range of quantum and magnetic systems.

Acknowledgements

The authors thank M. L. Rappaport for technical assistance. This work was supported by the European Research Council (ERC) under the European Union’s Horizon 2020 research and innovation program (grants No 785971 and 802952), by the US-Israel Binational Science Foundation (BSF) (grant No 2014155), and by the Weston Nanophysics Challenge Fund. EZ acknowledges the support of the Leona M. and Harry B. Helmsley Charitable Trust grant 2018PG-ISL006.

References

1. E. Persky and B. Kalisky, "Scanning SQUID View of Oxide Interfaces", *Adv. Mater.* **30**, 1706653 (2018).
2. F. Casola, T. van der Sar, and A. Yacoby, "Probing condensed matter physics with magnetometry based on nitrogen-vacancy centres in diamond", *Nat. Rev. Mater.* **3**, 17088 (2018).
3. L. Angeloni, M. Reggente, D. Passeri, M. Natali, and M. Rossi, "Identification of nanoparticles and nanosystems in biological matrices with scanning probe microscopy", *Wiley Interdiscip. Rev. Nanomedicine Nanobiotechnology* **10**, e1521 (2018).
4. F. Yang, A. J. Kollár, S. F. Taylor, R. W. Turner, and B. L. Lev, "Scanning Quantum Cryogenic Atom Microscope", *Phys. Rev. Appl.* **7**, 034026 (2017).
5. M. S. Grinolds, S. Hong, P. Maletinsky, L. Luan, M. D. Lukin, R. L. Walsworth, and A. Yacoby, "Nanoscale magnetic imaging of a single electron spin under ambient conditions", *Nat Phys* **9**, 215 (2013).
6. L. Thiel, D. Rohner, M. Ganzhorn, P. Appel, E. Neu, B. Müller, R. Kleiner, D. Koelle, and P. Maletinsky, "Quantitative nanoscale vortex imaging using a cryogenic quantum magnetometer", *Nat. Nanotechnol.* **11**, 677 (2016).
7. K. Chang, A. Eichler, J. Rhensius, L. Lorenzelli, and C. L. Degen, "Nanoscale Imaging of Current Density with a Single-Spin Magnetometer", *Nano Lett.* **17**, 2367 (2017).
8. L. Thiel, Z. Wang, M. A. Tschudin, D. Rohner, I. Gutiérrez-Lezama, N. Ubrig, M. Gibertini, E. Giannini, A. F. Morpurgo, and P. Maletinsky, "Probing magnetism in 2D materials at the nanoscale with single spin microscopy", *Science* **364**, 973 (2019).
9. J. R. Kirtley, M. B. Ketchen, K. G. Stawiasz, J. Z. Sun, W. J. Gallagher, S. H. Blanton, and S. J. Wind, "High-resolution scanning SQUID microscope", *Appl. Phys. Lett.* **66**, 1138 (1995).
10. A. G. P. Troeman, H. Derking, B. Borger, J. Pleikies, D. Veldhuis, and H. Hilgenkamp, "NanoSQUIDs based on niobium constrictions", *Nano Lett.* **7**, 2152 (2007).
11. D. Hazra, J. R. Kirtley, and K. Hasselbach, "Nano-superconducting quantum interference devices with continuous read out at milliKelvin temperatures", *Appl. Phys. Lett.* **103**, (2013).
12. J. R. Kirtley, L. Paulius, A. J. Rosenberg, J. C. Palmstrom, C. M. Holland, E. M. Spanton, D. Schiessl, C. L. Jermain, J. Gibbons, Y.-K.-K. Fung, M. E. Huber, D. C. Ralph, M. B. Ketchen, G. W. Gibson, and K. A. Moler, "Scanning SQUID susceptometers with sub-micron spatial resolution", *Rev. Sci. Instrum.* **87**, 093702 (2016).
13. P. Reith and H. Hilgenkamp, "Analysing magnetism using scanning SQUID microscopy", *Rev. Sci. Instrum.* **88**, 123706 (2017).
14. D. Vasyukov, Y. Anahory, L. Embon, D. Halbertal, J. Cuppens, L. Neeman, A. Finkler, Y. Segev, Y. Myasoedov, M. L. Rappaport, M. E. Huber, and E. Zeldov, "A scanning superconducting quantum interference device with single electron spin sensitivity", *Nat. Nanotechnol.* **8**, 639 (2013).
15. F. Foroughi, J.-M. Mol, T. Müller, J. R. Kirtley, K. A. Moler, and H. Bluhm, "A micro-SQUID with dispersive readout for magnetic scanning microscopy", *Appl. Phys. Lett.* **112**, 252601 (2018).
16. X. R. Wang, C. J. Li, W. M. Lu, T. R. Paudel, D. P. Leusink, M. Hoek, N. Poccia, A. Vailionis, T.

- Venkatesan, J. M. D. Coey, E. Y. Tsymbal, Ariando, and H. Hilgenkamp, "Imaging and control of ferromagnetism in LaMnO₃/SrTiO₃ heterostructures", *Science* **349**, 716 (2015).
17. D. Schmid-Lorch, T. Häberle, F. Reinhard, A. Zappe, M. Slota, L. Bogani, A. Finkler, and J. Wrachtrup, "Relaxometry and Dephasing Imaging of Superparamagnetic Magnetite Nanoparticles Using a Single Qubit", *Nano Lett.* **15**, 4942 (2015).
 18. Y. Anahory, L. Embon, C. J. Li, S. Banerjee, A. Meltzer, H. R. Naren, A. Yakovenko, J. Cuppens, Y. Myasoedov, M. L. Rappaport, M. E. Huber, K. Michaeli, T. Venkatesan, Ariando, and E. Zeldov, "Emergent nanoscale superparamagnetism at oxide interfaces", *Nat. Commun.* **7**, 12566 (2016).
 19. L. Embon, Y. Anahory, Ž. L. Jelić, E. O. Lachman, Y. Myasoedov, M. E. Huber, G. P. Mikitik, A. V. Silhanek, M. V. Milošević, A. Gurevich, and E. Zeldov, "Imaging of super-fast dynamics and flow instabilities of superconducting vortices", *Nat. Commun.* **8**, 85 (2017).
 20. D. Vasyukov, L. Ceccarelli, M. Wyss, B. Gross, A. Schwarb, A. Mehlin, N. Rossi, G. Tütüncüoğlu, F. Heimbach, R. R. Zamani, A. Kovács, A. Fontcuberta i Morral, D. Grundler, and M. Poggio, "Imaging Stray Magnetic Field of Individual Ferromagnetic Nanotubes", *Nano Lett.* **18**, 964 (2018).
 21. K. C. Nowack, E. M. Spanton, M. Baenninger, M. König, J. R. Kirtley, B. Kalisky, C. Ames, P. Leubner, C. Brüne, H. Buhmann, L. W. Molenkamp, D. Goldhaber-Gordon, and K. A. Moler, "Imaging currents in HgTe quantum wells in the quantum spin Hall regime", *Nat. Mater.* **12**, 787 (2013).
 22. E. M. Spanton, K. C. Nowack, L. Du, G. Sullivan, R.-R. Du, and K. A. Moler, "Images of Edge Current in InAs/GaSb Quantum Wells", *Phys. Rev. Lett.* **113**, 026804 (2014).
 23. A. Kremen, S. Wissberg, N. Haham, E. Persky, Y. Frenkel, and B. Kalisky, "Mechanical Control of Individual Superconducting Vortices", *Nano Lett.* **16**, 1626 (2016).
 24. D. V. Christensen, Y. Frenkel, Y. Z. Chen, Y. W. Xie, Z. Y. Chen, Y. Hikita, A. Smith, L. Klein, H. Y. Hwang, N. Pryds, and B. Kalisky, "Strain-tunable magnetism at oxide domain walls", *Nat. Phys.* **15**, 269 (2019).
 25. A. Finkler, Y. Segev, Y. Myasoedov, M. L. Rappaport, L. Ne'eman, D. Vasyukov, E. Zeldov, M. E. Huber, J. Martin, and A. Yacoby, "Self-aligned nanoscale SQUID on a tip", *Nano Lett.* **10**, 1046 (2010).
 26. Y. Anahory, J. Reiner, L. Embon, D. Halbertal, A. Yakovenko, Y. Myasoedov, M. L. Rappaport, M. E. Huber, and E. Zeldov, "Three-Junction SQUID-on-Tip with Tunable In-Plane and Out-of-Plane Magnetic Field Sensitivity", *Nano Lett.* **14**, 6481 (2014).
 27. L. Embon, Y. Anahory, A. Suhov, D. Halbertal, J. Cuppens, A. Yakovenko, A. Uri, Y. Myasoedov, M. L. Rappaport, M. E. Huber, A. Gurevich, and E. Zeldov, "Probing dynamics and pinning of single vortices in superconductors at nanometer scales", *Sci. Rep.* **5**, 7598 (2015).
 28. E. O. Lachman, A. F. Young, A. Richardella, J. Cuppens, H. R. Naren, Y. Anahory, A. Y. Meltzer, A. Kandala, S. Kempinger, Y. Myasoedov, M. E. Huber, N. Samarth, and E. Zeldov, "Visualization of superparamagnetic dynamics in magnetic topological insulators", *Sci. Adv.* **1**, e1500740 (2015).
 29. E. O. Lachman, M. Mogi, J. Sarkar, A. Uri, K. Bagani, Y. Anahory, Y. Myasoedov, M. E. Huber, A. Tsukazaki, M. Kawasaki, Y. Tokura, and E. Zeldov, "Observation of superparamagnetism in coexistence with quantum anomalous Hall $C = \pm 1$ and $C = 0$ Chern states", *npj Quantum*

- Mater.* **2**, 70 (2017).
30. D. Halbertal, J. Cuppens, M. Ben Shalom, L. Embon, N. Shadmi, Y. Anahory, H. R. Naren, J. Sarkar, A. Uri, Y. Ronen, Y. Myasoedov, L. S. Levitov, E. Joselevich, A. K. Geim, and E. Zeldov, "Nanoscale thermal imaging of dissipation in quantum systems", *Nature* **539**, 407 (2016).
 31. D. Halbertal, M. Ben Shalom, A. Uri, K. Bagani, A. Y. Meltzer, I. Marcus, Y. Myasoedov, J. Birkbeck, L. S. Levitov, A. K. Geim, and E. Zeldov, "Imaging resonant dissipation from individual atomic defects in graphene", *Science* **358**, 1303 (2017).
 32. J. Clarke and A. I. Braginski, Eds., *The SQUID Handbook*. Weinheim, FRG: Wiley-VCH Verlag GmbH & Co. KGaA, 2004.
 33. M. Tinkham, *Introduction to Superconductivity*, 2nd ed.,. McGraw-Hill, 1996.
 34. M. B. Ketchen, D. D. Awschalom, W. J. Gallagher, A. W. Kleinsasser, R. L. Sandstrom, J. R. Rozen, and B. Bumble, "Design, fabrication, and performance of integrated miniature SQUID susceptometers", *IEEE Trans. Magn.* **25**, 1212 (1989).
 35. A. Uri, A. Y. Meltzer, Y. Anahory, L. Embon, E. O. Lachman, D. Halbertal, N. HR, Y. Myasoedov, M. E. Huber, A. F. Young, and E. Zeldov, "Electrically Tunable Multiterminal SQUID-on-Tip", *Nano Lett.* **16**, 6910 (2016).
 36. L. Bickford Jr, "Ferromagnetic Resonance Absorption in Magnetite Single Crystal", *Phys. Rev.* **78**, 449 (1950).
 37. L. R. Bickford, "The low temperature transformation in ferrites", *Rev. Mod. Phys.* **25**, 75 (1953).
 38. G. Singh, H. Chan, A. Baskin, E. Gelman, N. Repnin, P. Král, and R. Klajn, "Self-assembly of magnetite nanocubes into helical superstructures", *Science* **345**, 1149 (2014).
 39. G. Singh, H. Chan, T. Udayabhaskararao, E. Gelman, D. Peddis, A. Baskin, G. Leitius, P. Král, and R. Klajn, "Magnetic field-induced self-assembly of iron oxide nanocubes", *Faraday Discuss.* **181**, 403 (2015).
 40. F. Walz, "The Verwey transition - a topical review", *J. Phys. Condens. Matter* **14**, R285 (2002).
 41. J. P. Wright, J. P. Attfield, and P. G. Radaelli, "Long Range Charge Ordering in Magnetite Below the Verwey Transition", *Phys. Rev. Lett.* **87**, 266401 (2001).
 42. M. S. Senn, J. P. Wright, and J. P. Attfield, "Charge order and three-site distortions in the Verwey structure of magnetite", *Nature* **481**, 173 (2012).
 43. P. Poddar, T. Fried, and G. Markovich, "First-order metal-insulator transition and spin-polarized tunneling in Fe₃O₄ nanocrystals", *Phys. Rev. B* **65**, 172405 (2002).
 44. Q. Yu, A. Mottaghizadeh, H. Wang, C. Ulysse, A. Zimmers, V. Rebutini, N. Pinna, and H. Aubin, "Verwey transition in single magnetite nanoparticles", *Phys. Rev. B* **90**, 075122 (2014).
 45. J. Lee, S. G. Kwon, J.-G. Park, and T. Hyeon, "Size Dependence of Metal–Insulator Transition in Stoichiometric Fe₃O₄ Nanocrystals", *Nano Lett.* **15**, 4337 (2015).
 46. A. Hevroni, M. Bapna, S. Piotrowski, S. A. Majetich, and G. Markovich, "Tracking the Verwey Transition in Single Magnetite Nanocrystals by Variable-Temperature Scanning Tunneling Microscopy", *J. Phys. Chem. Lett.* **7**, 1661 (2016).
 47. N. T. H. Kim-Ngan and W. Soszka, "The surface metal-insulator transition in MBE magnetite

- thin films", *Phys. B Condens. Matter* **319**, 133 (2002).
48. M. Zając, K. Freindl, T. Ślęzak, M. Ślęzak, N. Spiridis, D. Wilgocka-Ślęzak, and J. Korecki, "Electronic and magnetic properties of ultra-thin epitaxial magnetite films on MgO(001)", *Thin Solid Films* **519**, 5588 (2011).
 49. M. E. Schabes and H. N. Bertram, "Magnetization processes in ferromagnetic cubes", *J. Appl. Phys.* **64**, 1347 (1988).
 50. P. Guardia, A. Labarta, and X. Batlle, "Tuning the Size, the Shape, and the Magnetic Properties of Iron Oxide Nanoparticles", *J. Phys. Chem. C* **115**, 390 (2011).
 51. J. Baumgartner, L. Bertinetti, M. Widdrat, A. M. Hirt, and D. Faivre, "Formation of Magnetite Nanoparticles at Low Temperature: From Superparamagnetic to Stable Single Domain Particles", *PLoS One* **8**, e57070 (2013).
 52. M. Jamet, W. Wernsdorfer, C. Thirion, D. Mailly, V. Dupuis, P. Mélinon, and A. Pérez, "Magnetic anisotropy of a single cobalt nanocluster", *Phys. Rev. Lett.* **86**, 4676 (2001).
 53. C. Thirion, W. Wernsdorfer, and D. Mailly, "Switching of magnetization by nonlinear resonance studied in single nanoparticles", *Nat. Mater.* **2**, 524 (2003).
 54. W. Wernsdorfer, "Classical and Quantum Magnetization Reversal Studied in Nanometer-Sized Particles and Clusters", in *Advances in Chemical Physics*, 2007, 99.
 55. W. Wernsdorfer, "From micro- to nano-SQUIDs: applications to nanomagnetism", *Supercond. Sci. Technol.* **22**, 064013 (2009).
 56. M. J. Martínez-Pérez, B. Müller, D. Schwebius, D. Korinski, R. Kleiner, J. Sesé, and D. Koelle, "NanoSQUID magnetometry of individual cobalt nanoparticles grown by focused electron beam induced deposition", *Supercond. Sci. Technol.* **30**, 024003 (2017).
 57. M. J. Martínez-Pérez, J. Pablo-Navarro, B. Müller, R. Kleiner, C. Magén, D. Koelle, J. M. De Teresa, and J. Sesé, "NanoSQUID Magnetometry on Individual As-grown and Annealed Co Nanowires at Variable Temperature", *Nano Lett.* **18**, 7674 (2018).
 58. A. Finkler, D. Vasyukov, Y. Segev, L. Ne'eman, E. O. Lachman, M. L. Rappaport, Y. Myasoedov, E. Zeldov, and M. E. Huber, "Scanning superconducting quantum interference device on a tip for magnetic imaging of nanoscale phenomena", *Rev. Sci. Instrum.* **83**, 073702 (2012).
 59. A. Marguerite, J. Birkbeck, A. Aharon-Steinberg, D. Halbertal, K. Bagani, I. Marcus, Y. Myasoedov, A. K. Geim, D. J. Perello, and E. Zeldov, "Imaging work and dissipation in the quantum Hall state in graphene", *Nature* **575**, 628 (2019).
 60. A. Uri, Y. Kim, K. Bagani, C. K. Lewandowski, S. Grover, N. Auerbach, E. O. Lachman, Y. Myasoedov, T. Taniguchi, K. Watanabe, J. Smet, and E. Zeldov, "Nanoscale imaging of equilibrium quantum Hall edge currents and of the magnetic monopole response in graphene", *Nat. Phys.* in press (2019) doi:10.1038/s41567-019-0713-3.
 61. K. J. M. Bishop, C. E. Wilmer, S. Soh, and B. A. Grzybowski, "Nanoscale Forces and Their Uses in Self-Assembly", *Small* **5**, 1600 (2009).
 62. K. Abe, Y. Miyamoto, and S. Chikazumi, "Magnetocrystalline Anisotropy of Low Temperature Phase of Magnetite", *J. Phys. Soc. Japan* **41**, 1894 (1976).

Supplementary information

SQUID-on-tip with single-electron spin sensitivity for high-field and ultra-low temperature nanomagnetic imaging

Y. Anahory^{1*}, H.R. Naren², E.O. Lachman², S. Buhbut Sinai³, A. Uri²,
L. Embon², E. Yaakobi², Y. Myasoedov², M.E. Huber⁴, R. Klajn³ and E. Zeldov²

¹Racah Institute of Physics, The Hebrew University, Jerusalem 91904, Israel

²Department of Condensed Matter Physics, Weizmann Institute of Science, Rehovot 7610001, Israel

³Department of Organic Chemistry, Weizmann Institute of Science, Rehovot 7610001, Israel

⁴Departments of Physics and Electrical Engineering, University of Colorado Denver, Denver 80217, USA

*Corresponding author: yonathan.anahory@mail.huji.ac.il

Measurement of I-V characteristics

The measurement circuit, illustrated schematically in Fig. S1, consists of a room temperature voltage source that provides the bias current I_B through the low temperature bias resistor R_B , with a typical value of a few k Ω . The SOT is effectively voltage-biased by the low-resistance shunt resistor R_S , with a value of a few Ω , in presence of a parasitic resistance R_p . The current through the SOT, I_{SOT} , was measured using a SQUID series array amplifier (SSAA) as described in Refs.^{1,2} and identified in Fig. S1 as A. The SSAA is inductively coupled to the SOT circuit through a superconducting coil L_{in} . Warm electronics applies a voltage V_{FB} to maintain a constant flux in the SSAA. In flux-locked loop conditions, $I_{FB} \propto I_{SOT}$ and I_{FB} is itself proportional to the voltage drop V_{FB} on a resistor R_{FB} , with a typical value of a few k Ω . Thus, V_{FB} is a direct readout of I_{SOT} .

Figure S2a,c,e shows the raw I_{SOT} - I_B curves of a SOTs at 300 mK for different materials. The I_{SOT} - I_B curves can be separated into two regions. Below I_c , a linear region with slope $R_S/(R_S + R_p)$ represents the state where the SOT is superconducting. For larger values of I_B , the SOT is in the voltage state and the curve is no longer linear. Knowing the voltage on the shunt resistor $V_S = R_S(I_B - I_{SOT})$, and the voltage on the parasitic resistance $V_p = R_p I_{SOT}$, we calculate $V_{SOT} = V_S - V_p$. From this result, we can then present the I_{SOT} - V_{SOT} curves (Fig. S2 b,e,f).

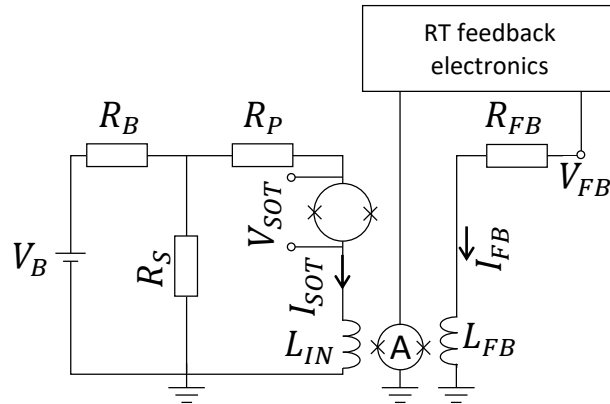


Figure S1 – Detailed measurement circuit. R_B and R_{FB} are typically a few k Ω , R_S a few ohms, and R_p ideally below 1 ohm. All of the circuit except for the room-temperature feedback electronics is at 300 mK.

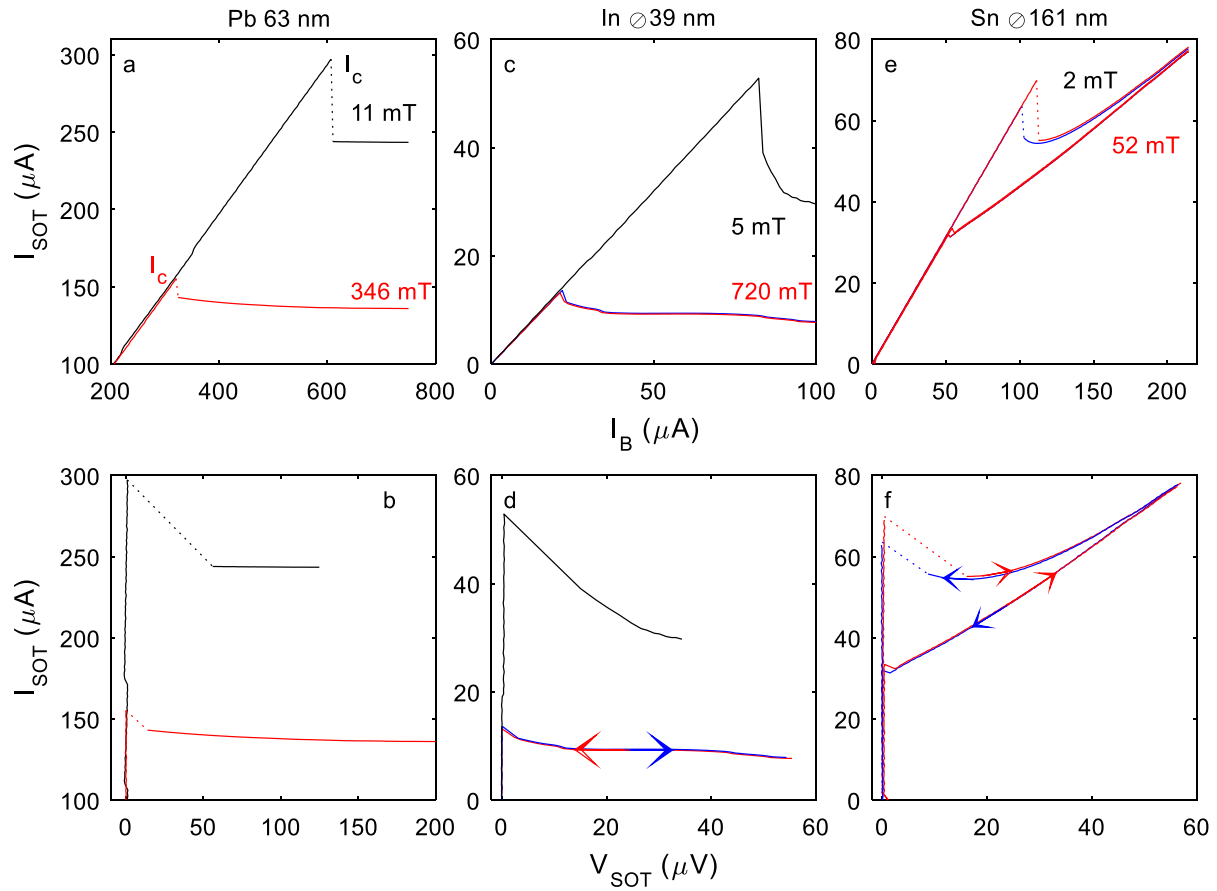


Figure S2 - I - V characteristics of SOT devices made of different materials at 300 mK. (a-f) I - V characteristics of three different SOT devices at two different applied magnetic fields. (a) I_{SOT} - I_B curve of a hysteretic unshunted Pb SOT with diameter of 63 nm ($R_B = 2.0$ k Ω , $R_S = 3.0$ Ω , $R_P = 3.1$ Ω). (b) The corresponding I_{SOT} - V_{SOT} characteristics of the Pb device. (c) I_{SOT} - I_B characteristics of an In SOT of 39 nm diameter with integrated shunt-on-tip ($R_B = 7.0$ k Ω , $R_S = 3.0$ Ω , $R_P = 1.8$ Ω) and its corresponding I_{SOT} - V_{SOT} characteristics (d). The red (blue) curve shows the measurement upon ramping I_B up (down). (e) I_{SOT} - I_B characteristics of a slightly hysteretic shunted Sn SOT with diameter of 162 nm ($R_B = 7.0$ k Ω , $R_S = 3.0$ Ω , $R_P = 1.8$ Ω) with its corresponding I_{SOT} - V_{SOT} characteristics (f). The inset shows a simplified diagram of the measurement circuit.

Additional Fe₃O₄ nanocube images at zero field

Small particles such as Fe₃O₄ nanocubes can have defects that might influence the observations in this work. Here we show four other nanocubes that were imaged with the same 150 nm diameter In SOT as in the main text at the same temperature of about 300 mK. These images were also taken after ramping the field to 0.36 T. The out-of-plane field $B_z(x, y)$ images are shown in Fig. S3 a-c. For each of the images, the magnitude of the magnetic moment, m_0 , as well as its polar, θ , and azimuthal, ϕ , angles were derived by performing a numerical fit of the data. Our model comprises a finite size SQUID loop with fitting parameters m_0 , θ , ϕ and the SOT-to-nanocube distance. The corresponding numerically attained best-fit stray field maps are presented in Figs. S3 d-f. The subtraction of the experimental and the corresponding best-fit image to show the quality of the fit is shown in Figs. S3 g-i. The magnitude and the polar angle are consistent with the finding shown in the main text. We have no evidence of other nanocubes behaving in a significantly different manner.

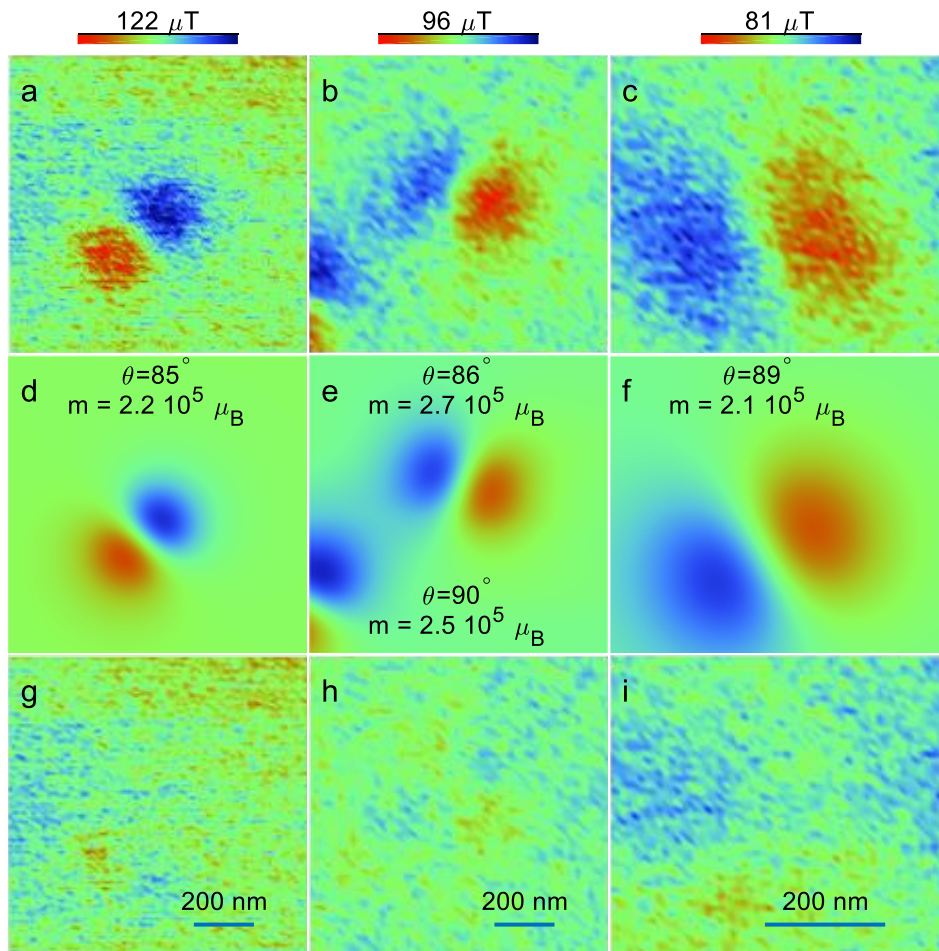


Figure S3 - Additional images at zero field – (a-c) Stray field $B_z(x, y)$ of different Fe₃O₄ nanocube at $\mu_0 H_z = 0$ T. (d-e) Corresponding best fit numerically simulated $B_z(x, y)$ with magnetic moment and polar angle found for each nanocube. The best tip-to-sample distance fit was 141 (d), 171 (e) and 165 nm (f) (g-h) Subtraction of the experimental image and the corresponding fit.

References

1. A. Finkler, Y. Segev, Y. Myasoedov, M. L. Rappaport, L. Ne'eman, D. Vasyukov, E. Zeldov, M. E. Huber, J. Martin, and A. Yacoby, "Self-aligned nanoscale SQUID on a tip", *Nano Lett.* **10**, 1046 (2010).
2. D. Vasyukov, Y. Anahory, L. Embon, D. Halbertal, J. Cuppens, L. Neeman, A. Finkler, Y. Segev, Y. Myasoedov, M. L. Rappaport, M. E. Huber, and E. Zeldov, "A scanning superconducting quantum interference device with single electron spin sensitivity", *Nat. Nanotechnol.* **8**, 639 (2013).